The low-temperature sonochemical synthesis of up-converting β $NaYF_4$:Yb,Er mesocrystals

Marina Vukovic[1], Ivana Dinic[2], Paula Jardim[3], Smilja Markovic[2], Ljiljana Veselinovic[2], Marko Nikolic[4], Lidija Mancic[2]

[1]Innovative Centre, Faculty of Chemistry, University of Belgrade – Serbia

[2]Institute of Technical Sciences of Serbian Academy of Science and Arts, Belgrade, Serbia

[3] Department of Metallurgical and Materials Engineering, Federal University of Rio de Janeiro, Rio de Janeiro, Brazil

[4]Photonic Center, Institute of Physics Belgrade, University of Belgrade, Serbia

[*]Corresponding autor: Lidija Mancic, lidija.mancic@itn.sanu.ac.rs

Abstract

In this paper, we report the mild sonochemical synthesis of hexagonal (β) $NaYF_4$:Yb,Er mesocrystals at low temperature of 40 °C. The nucleation and transformation of crystal structures is investigated in the course of time, and it is shown that the pure β phase is obtained after 2 h of pulsed sonication. The crystallization of orthorhombic YF_3:Yb,Er and cubic (α) $NaYF_4$:Yb,Er precedes the appearance of a thermodynamically stable β $NaYF_4$:Yb,Er phase. Based on the evolution of the nanoparticle morphology, it is concluded that the transition from α to β phase is consistent with the dissolution-recrystallization process, while the final shape of mesocrystals is a consequence of the oriented attachment growth in the newly formed β phase nanocrystallites along two planes. The structural properties of all compounds are analyzed and correlated with their thermal and optical characteristics. The pump power dependence of green and red emissions confirms that only two-photon process is involved in up-conversion, which is superior in β phase mesocrystals.

Keywords: sonochemistry; $NaYF_4$:Yb,Er; YF_3:Yb,Er; mesocrystals; up-conversion;

Introduction

Up-conversion (UC) is a non-linear optical process that transforms low-energy photons into high-energy photons, thus enabling the emission of multiple colors upon the excitation of an optically active material with near-infrared (NIR) light. Efficient UC is closely related to rare earth (RE) doped inorganic compounds (oxides, halides and sulfides) which have a high refractive index and low phonon energy of about 350 cm^{-1}. It is widely recognized that the most promising UC material today is hexagonal (β) $NaYF_4$:Yb,Er. This phase is characterized by a higher degree of crystal asymmetry and multisite dopant accommodation, positioned at a shorter distance in a crystal cell than ones of the cubic (α) phase [1]. The synthesis of the β phase through the decomposition of the corresponding organometallic precursors in an oleic acid/oleylamine/octadecane solvent mixture [2] is a well established and widely exploited procedure which yields hydrophobic UC nanoparticles with a uniform size. Quite the contrary, for the straightforward synthesis of hydrophilic RE fluorides surfactant-assisted hydro- and solvo-thermal methods are deemed to be the most effective strategies [3]. Among others, we have also shown that the alteration of the particle morphology, composition and crystal structure is achievable through temperature and time control [4] or through addition of different polymers and solvents during the hydrothermal processing of YF_3:Yb,Er and $NaYF_4$;Yb,Er phase [5]. Some other method, like polyol-mediated synthesis at a high temperature is reported to be beneficial in the synthesis of well crystalline UC nano- and micro-crystals [6]. Since the overall efficiency of the UC process depends on a cascade of events in the host material [7], fine tuning of the processing parameters is crucial for obtaining RE fluorides that could be used in solid-state lasers [8], thermometry [9], cell labeling [10], solar cells [11], etc.

Ultrasonication is widely used for the modification of solids, synthesis of nanoparticles, exfoliation of layered materials or dispersion of particles in different matrices [12]. It is based on

acoustic cavitation, i.e. the formation, growth and implosive collapse of microbubbles in a very short time. Passing of ultrasonic waves through a liquid medium causes high-speed impinging liquid jets and strong hydrodynamic shear forces. An enhanced mass transfer and local thermal heating additionally contribute to accelerated nucleation and growth of nanoparticles, promoting the diffusion of dopants into the host material and, consequently, increasing the quantum yield of photoluminescence [13]. Still, there are only a few reports on the sonochemical synthesis of RE fluorides. For example, dumbbell-like YF_3 nanostructures have been prepared starting from Y_2O_3 and NH_4F in a mixture of diluted HNO_3 and DMF at 65 °C for 2h [14], while hydrofluoric acid and argon atmosphere are used for the processing of needle-shaped YF_3 nanoparticles from yttrium acetate at 25 °C for 1 h [15]. Luminescent CeF_3 nanoparticles doped with a variety of lanthanide ions (like Dy^{3+}, Eu^{3+}, and Tb^{3+}) are obtained after 100 min of continuous sonication of the corresponding RE nitrates and potassium tetrafluoroboride solution [16], whilst ultrasmall LaF_3:Ce,Tb nanoparticles are stabilized in tetraethylene glycol/1-butyl-3 methylimidazoliumtetrafluoroborate reaction mixture after 10 min pulsed irradiation at 100 °C [17]. For the synthesis of doubly doped YF_3 and $NaYF_4$ nanoparticles, pulsed irradiation needs to be much longer and require use of nitrogen or argon protective atmosphere, but even then, efficient UC emission is detected only after an additional annealing of the obtained particles [18]. Although these RE fluorides have different compositions, all of them were obtained from organic precursors and solvents under strictly controlled temperature, atmosphere, ultrasonic power and the sonication regime. The objective of this study is to present a mild sonochemical synthesis of the β $NaYF_4$:Yb,Er phase through irradiation of a common mixture of corresponding nitrates and sodium fluoride in air. In addition, the evolution process of YF_3:Yb,Er and α $NaYF_4$:Yb,Er, which precede the formation of a thermodynamically stable β phase, is investigated in order to reveal the mechanisms of their nucleation and subsequent α→ β transformation during sonication.

Experimental

All Sigma Aldrich reagents were of an analytical grade. First, the defined stoichiometric amounts of rare earth nitrates (5 mmol in total) were dissolved in 50 ml of deionized water and pH was adjusted to 3 using HNO_3. Then, 50 ml of the NaF solution (RE:F= 1:6) were prepared and pH was adjusted to 10 using NaOH. Thus, the obtained solutions were mixed together and transferred into a standard sonochemical reaction glass vessel. The reaction mixture was irradiated with ultrasonic waves of 20 kHz by a Vibra Cell VCX750 Sonic ultrasound processor at 60% of power. A titanium alloy solid tip, 13 mm wide, was used in a 2:1 s pulse regime for 30, 60, 90 and 120 min without protective atmosphere. The temperature of the solution was kept at 40 °C. After the ultrasonic treatment, the samples with a nominal composition $NaY_{0.8}F_4$:$Yb_{0.18}Er_{0.02}$ were collected by centrifugation at 7000 rpm, rinsed 3 times with deionized water and dried at 80 °C for 3 h. According to the reaction time, the samples were named S30, S60, S90 and S120, respectively.

X-ray powder diffraction (XRPD) patterns were recorded on Rigaku SmartLab diffractometer, equipped with a Cu-Kα source (λ= 1.5406 Å) using a scanning rate of 0.01 °/s. The structural data for the particles were acquired through combined La Bail and Rietveld refinement in the Topas 4.2 software [19]. For the β $NaYF_4$ hexagonal phase, refinement was carried out in the P63/m (No.176) space group using the Fundamental Parameter approach. An isotropic size-strain analysis was performed using a predefined double-Voigt approach (volume weighted mean column height, FWHM based LVol). The sherical harmonic formulation, also known as “orientation distribution function”, was included during the fitting of diffraction line intensity, due to the observed preferential growth. The morphological and crystallographic characteristics of the particles were investigated using field-emission scanning electron microscopy (Dualbeam Versa 3D FE-SEM), transmission electron microscopy and (TEM) and scanning transmission electron microscopy (STEM) associated with energy-dispersive X-ray

spectroscopy (EDS) (Titan G2 80-200 with ChemiSTEM technology). Fourier transform infrared spectroscopy (FT-IR) was done on a Nicolet iS10 FT-IR Spectrometer (Thermo Scientific) in the spectral range from 400 to 4000 cm^{-1}. Differential scanning calorimetry (DSC) measurements were performed on an Evo 131 (Setaram Instrumentation) differential scanning calorimeter. Samples of about 5 mg in weight were analyzed in nitrogen by heating (10 °C/min) from 25 °C to 550 °C. After the analysis, the samples were subjected to XRPD once again. Photoluminescence (PL) emission measurements were performed at room temperature using a TE-Cooled CCD Fluorescence spectrometer (Edmund Optics) and a 980 nm laser diode (1 W, Dragon Laser). To investigate the UC mechanism, PL emission intensity dependence on the pumping power was tracked using a PM16-22 Thorlabs Power Meter with a photodiode sensor.

Results and discussion

The XRPD patterns of the synthesized powders are presented in Figure 1. As it is indicated by indexed Bragg reflections, the samples obtained at shorter sonication times are multiphase. The presence of the α $NaYF_4$ (JCPDS 77-2042), β $NaYF_4$ (JCPDS 16-0334) and YF_3 (JCPDS 70-1935) phases is revealed in S30 and S60, whilst a broad hump (2θ: 20–60°) in the S90 pattern suggests the prevalence of the amorphous phase content over the crystalline phases. The structural refinement of XRPD patterns acquired through combined La Bail and Rietveld refinement are given in Supplementary file (Figure S1), while microstructural parameters obtained are given in Table 1. As one could see from Fig.1d, Fig. S1d and Table 1, the prolongation of sonication lead to pure β $NaYF_4$:Yb,Er formation in S120. The structural refinement of this phase has revealed that the introduction of dopants with smaller ionic radii (Y^{3+}:101.9 pm; Yb^{3+}:98.5 pm; Er^{3+}:100 pm) leads to a decrease in unit cell parameters and cell volume, whereas the mean crystallite size of 37.6(4) nm is accompanied with a high value of microstrain, 0.31(1), (Supplementary file, Table S1). From the kinetic point of view, the ordering of the β phase is a time and energy consuming process [20], whilst the conditions induced by

ultrasound generate high temperatures in the localized spots of the collapsing bubbles under extremely high heating and cooling rates [21]. Thus, the energy developed at collapse is sufficient for passing a barrier for crystallization of the β phase (the presence of this phase is proven in all samples), but the time for the relaxation of the obtained crystals is not. For this reason, in the samples obtained under shorter sonication, a kinetically stable α $NaYF_4$:Yb,Er phase is also present. Apart from that, the emergence of the YF_3:Yb,Er phase indicates that although fast, nucleation through the whole precursor volume is not homogeneous. According to the literature [22], in ultrasonically irradiated liquids a three-region sites for chemical reactions have been recognized (the cavitation bubble proper, the solution bulk and the bubble/solution interface), suggesting that nucleation depends on the region where the chemical reaction takes place. To suppress the nucleation of simple fluorides in micro-environmental spots where fluorine ions prevail over sodium ones, a sodium surplus providing through addition of $NaNO_3$ [23] and rising of cavitation temperature through sonication under argon atmosphere [18] have been reported. Here, we have shown for the first time that it is possible to obtain single-phase β $NaYF_4$:Yb,Er by simply extending the sonication time.

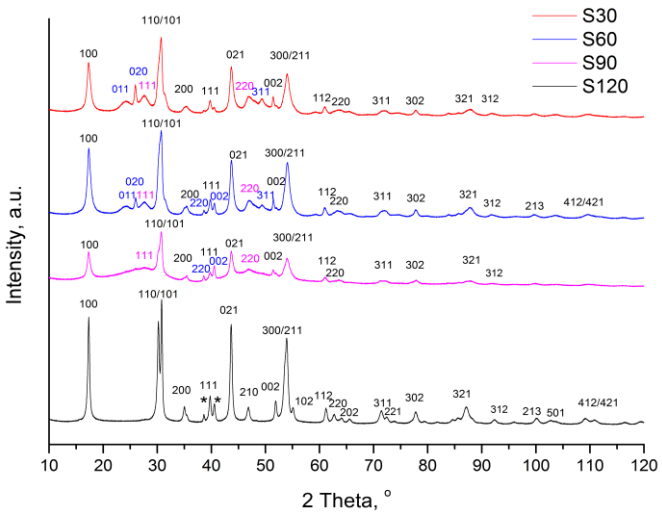

Figure 1. Comparative XRPD of samples obtained through sonochemical synthesis with assigned reflections of the Yb,Er doped: α-$NaYF_4$ (pink), β-$NaYF_4$ (black) and YF_3 (blue); two reflections in S120 marked with * originate from Ti contamination (titanium horn is used during synthesis)

Table 1. Crystal cell parameters of the samples obtained through sonochemistry

Sample	**S30**			**S60**			**S90**			**S120**
	$NaYF_4$:Yb,Er		YF_3:Yb,Er	$NaYF_4$:Yb,Er		YF_3:Yb,Er	$NaYF_4$:Yb,Er		YF_3:Yb,Er	$NaYF_4$:Yb,Er
S.G.	*Fm-3m*	*P6₃/m*	*Pnma*	*Fm-3m*	*P6₃/m*	*Pnma*	*Fm-3m*	*P6₃/m*	*Pnma*	*P6₃/m*
a, Å	5.513(1)	5.9043(1)	6.243(2)	5.489(2)	5.9027(3)	6.252(2)	5.506(5)	5.894(1)	6.369(37)	5.934(1)
b, Å			6.884(1)			6.879(1)			6.875(56)	
c, Å		3.5481(1)	4.573(1)		3.5492(2)	4.560(1)		3.542(2)	4.683(40)	3.529(1)
V, $Å^3$	167.56	107.12	196.53	165.38	107.09	196.11	166.92	106.56	205.05	107.61

α -$NaYF_4$ (JCPDS 77-204, cubic, Fm-3m): a=5.470Å V= 163.66 $Å^3$; β $Na_{1.5}Y_{1.5}F_6$ (JCPDS 16-0334, hexagonal, P63m): a=5.960Å c=3.530Å, V= 108.59 $Å^3$; YF_3 (JCPDS 70-1935, orthorhombic, Pnma): a=6.3537Å b=6.8545Å c=4.3953 , V= 191.42 $Å^3$;

The FE-SEM micrographs of the obtained particles are presented in Fig. 2. A spindle-like morphology prevails in all powders, except for S90, where micron-sized aggregates of very small particles dominate, Fig. 2c. These irregularly shaped fluffy aggregates probably correspond to the amorphous phase detected by the XRPD analysis. Spherical nanoparticles, although minor in terms of content, are also present in the samples obtained under a shorter sonication time. These spherical nanoparticles with diameters around 10 nm have been identified as the α $NaYF_4$:Yb,Er cubic phase through selected area electron diffraction (SAED) in a TEM analysis of the sample S30 (Fig. 3).

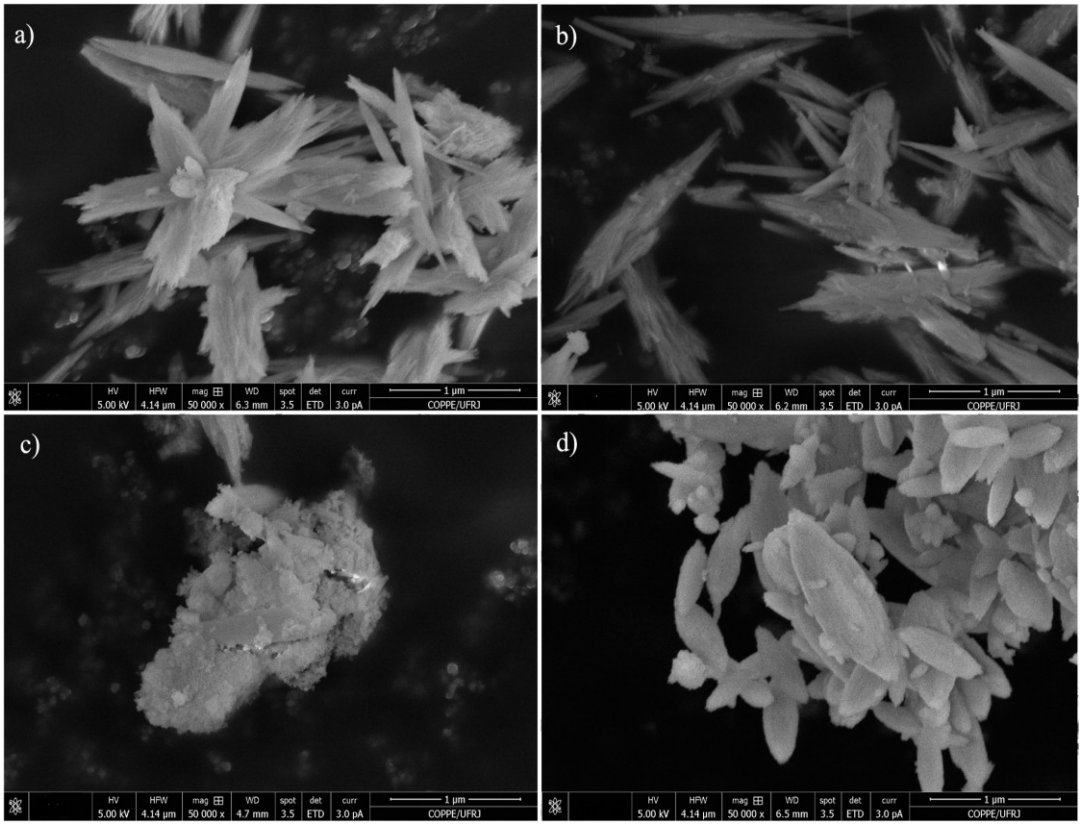

Figure 2. FE-SEM micrographs of S30 (a); S60 (b); S90 (c); and S120 (d)

The SAED analysis of randomly oriented spindle-like particles in S120 shows that they belong to the β $NaYF_4$:Yb,Er hexagonal phase (Fig. 4), which is in agreement with the XRPD results. High-resolution TEM images reveal that spindle-like particles in samples S30, S60 and S120 are mesocrystals formed of nanorod crystals with diameters around 10 nm (Fig. 5c). The FFT of high-resolution TEM images (Fig.5d) reveals that these mesocrystals could be indexed as the zone axis [-111] of the β $NaYF_4$:Yb,Er hexagonal phase with a preferential growth direction perpendicular to (1-12) planes. A typical SAED pattern of a single spindle-like mesocrystal is shown Fig. 5b. A comparison of this pattern with the SAED pattern of many randomly oriented spindle-like mesocrystal (Fig. 4) suggests the presence of a crystallographic texture of two overlain zone axes (ZA): [-111] with a growth direction along the direction perpendicular to (1-12) plane and [2-10] with a growth direction along [001]. Therefore, the orientation relationship (OR): (001)//(1-12) and [-111]//[2-10] of the β $NaYF_4$:Yb,Er hexagonal crystals forming the mesocrystal can be obtained from the interpretation of the diffraction pattern in Fig. 5 (more details on the SAED patterns indexation are shown in Fig. S4 and S5 in Supplementary file). This OR favors the formation of low energy coherent interfaces. This is clear from the SAED pattern (Fig. 5) showing planes with similar (or the same) interplanar distances parallel to each other. The [001] preferential growth direction of the β $NaYF_4$ hexagonal phase has already been reported in the literature [24,25]. The possible explanations for the presence of these two crystal orientations and growth directions for the β $NaYF_4$:Yb,Er hexagonal phase forming mesocrystals are a similar growth velocity along [001] and the direction perpendicular to (1-12) plane and the low energy interfaces formed between these two crystal orientations. In our study, the same SAED, and therefore the same OR between crystals forming the mesocrystals, has been observed for all spindle-like mesocrystals in the samples S30, S60 and S120. However, as one can see in Fig. 2, the spindle-like particles in the samples obtained at shorter reaction times (S30 and S60) are much more elongated (mean length, width and the aspect ratio of 1.5 μm, 139 nm and 10.7

respectively) than in S120 (mean length, width and the aspect ratio of 540 nm, 152 nm and 3.4 respectively). The presence of mesocrystals indicates that the orientation attachment growth mechanism, suggested earlier for hydrothermally synthesized β $NaYF_4$ self-assemblies [26], occurs here after a certain time of sonication. However, the evolution of different phases, as well as the morphology change (aspect ratio) of spindle-like mesocrystals during the reaction time, demonstrates that the dissolution/precipitation mechanism also influences their final shape. STEM/EDS maps show a homogeneous distribution of sodium, yttrium, ytterbium, erbium and fluorine in spindle-like mesocrystals (Fig.6). The EDS analysis also confirms the absence of titanium alloy horn contamination.

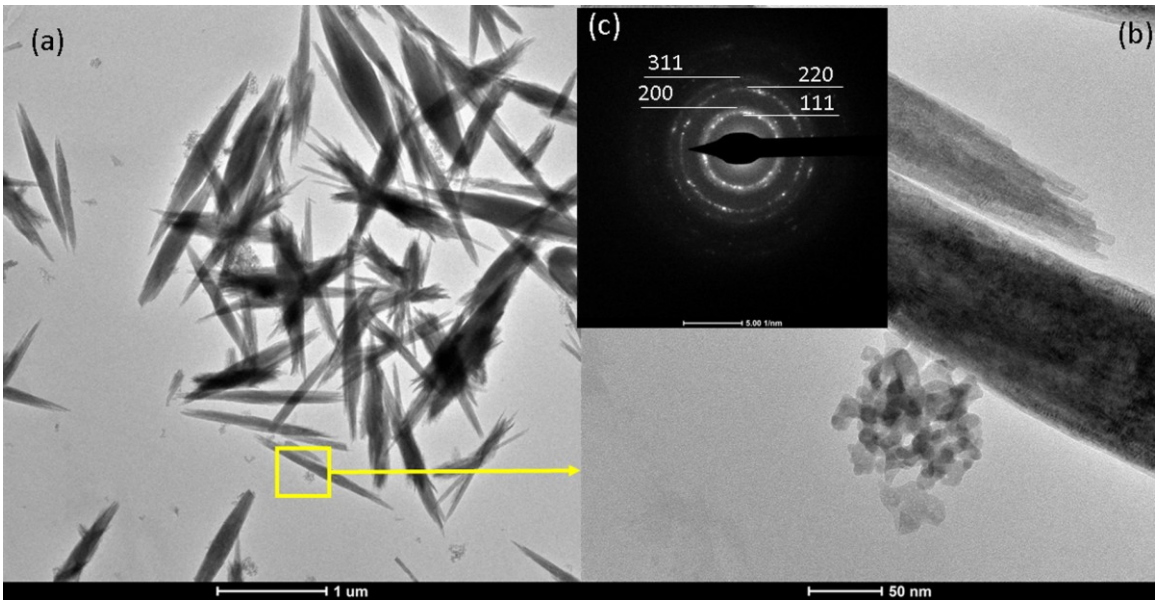

Figure 3. TEM images of S30 spindle-like and spherical nanoparticles (a,b) and the SAED (c) pattern of spherical particles identified as the α $NaYF_4$:Yb,Er cubic phase

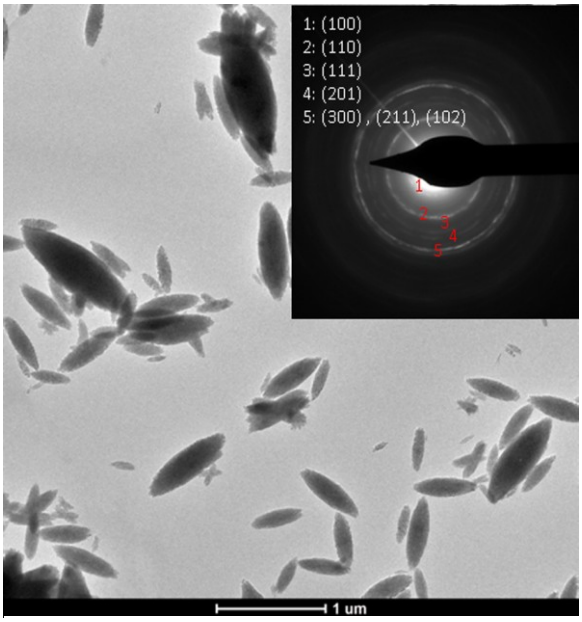

Figure 4. TEM image of the sample S120 and the corresponding SAED pattern

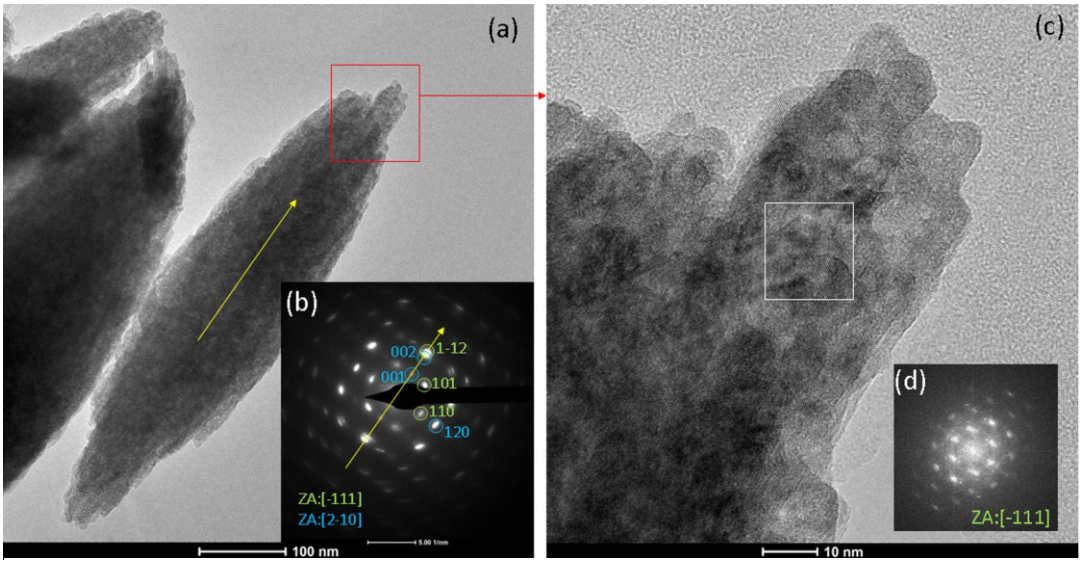

Figure 5. (a) TEM image of a spindle-like mesocrystal in the sample S120 and the corresponding SAED pattern (b) showing the growth direction (yellow arrow); (c) a higher magnification of the marked region in (a) and a FFT (d) of the region indicated in (c).

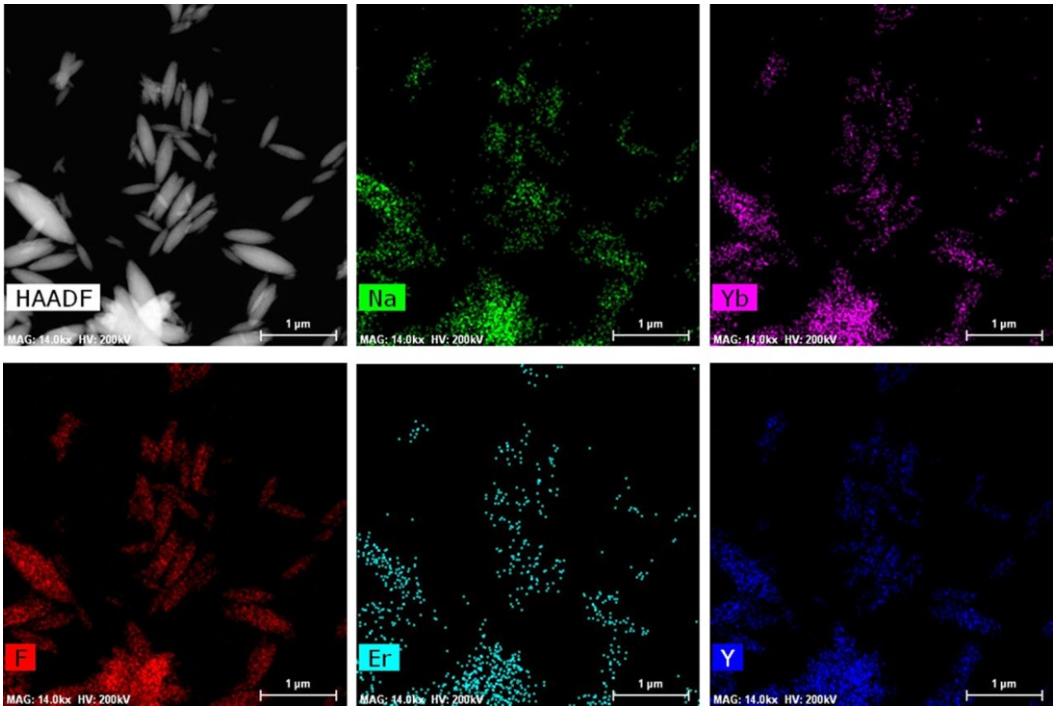

Figure 6: HAADF image and Na, Yb, F, Er and Y EDS maps of sample S120.

The surface properties of the particles were additionally tested in a FT-IR analysis. A typical spectrum, presented in Figure S2 (Supplementary file), confirms the high purity of the particles and the presence of adsorbed H_2O. Namely, the bands at 3500 cm^{-1} and 1650 cm^{-1} could be assigned to the asymmetric stretching and bending mode of adsorbed water [27].

To shed more light on the thermal stability of the studied samples, a DSC analysis was performed. In general, the thermodynamic properties of RE^{3+} doped $NaYF_4$ materials are rarely explored [28,29], while scarce data concerning the binary phase diagrams of alkali metal fluorides and RE^{3+} fluorides can be found in the literature [30,31]. As shown in Fig.7, the DSC curves of all samples have a similar trend. The adsorbed water is released first from the samples at low temperatures. In addition, at higher temperatures, two exothermal peaks are clearly detected in the samples. In accordance to the XRPD analysis of samples after DSC analysis (Figure S3, Supplementary file) the first peak at 324 °C, which is the most pronounced in S90 (shaded in Fig.7c, ΔH =58.2J/g), is associated with the further crystallization of the YF_3:Yb,Er. While this phase crystallize from the amorphous part of S30 (detected by XRPD and FESEM

analysis, Fig.1c and Fig. 2c), its appearance in the XRPD pattern of thermally treated S120 (Fig.S3d, Supplementary file) suggest that decomposition of the less stable β $NaYF_4$:Yb,Er nanocrystals (visible in Fig.4) occurred during DSC analysis. Presence of NaF is indicative, due to the appearance of its strongest reflection (200) at 2θ 38.8, Fig.S3d. The lower thermal stability of nanocrystals with anisotropic shape (in comparison to the stability of spherical nanocrystals of the same volume or anisotropic crystals with a bigger volume) is recently reported for α $NaYF_4$:Yb,Er [32], so we assume that same occurs with the β $NaYF_4$:Yb,Er nanocrystals. The second peak at 512 °C, the most pronounced in S30 (shaded in Fig.7a, ΔH=45.8J/g), is related to the cubic → hexagonal $NaYF_4$;Yb,Er phase transformation [33]. The calculated specific enthalpy (ΔH=45.8J/g) agrees well with the previously determined value for the α $NaYF_4$:Yb^{3+}:RE^{3+} phase transitions when RE^{3+} co-doping ions are other than Er, whilst the corresponding transition temperature determined here is a bit higher than reported [29]. This clearly implies the dependence of the α→ β phase transition temperature on the choice of dopants and on exact particle stoichiometry.

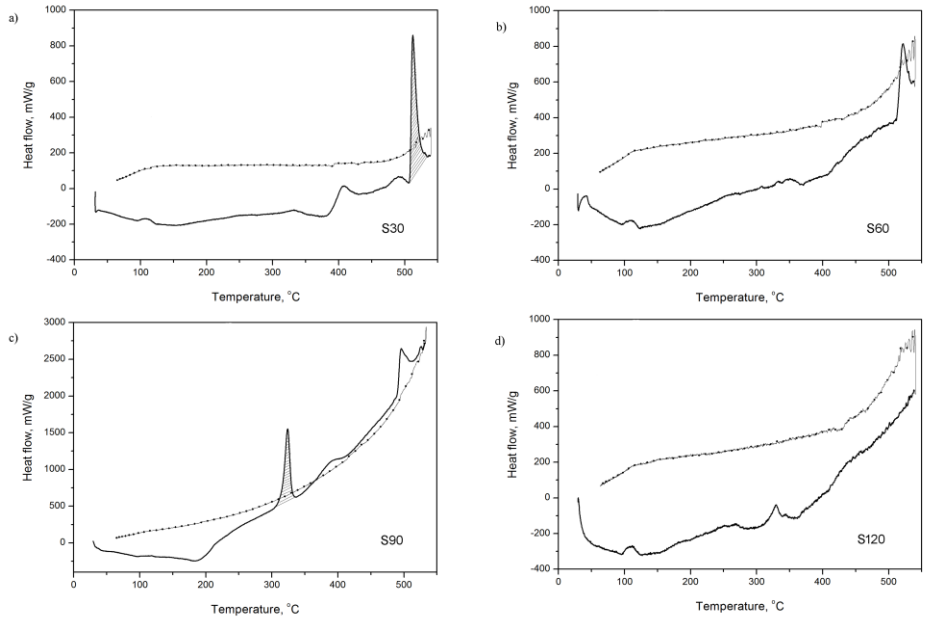

Figure 7. DSC curves of S30 (a); S60 (b); S90 (c); S120 (d); (heating-solid line, cooling-dash line)

The observed differences in the composition of the samples are reflected in their up-conversion spectra, Fig. 8a. The most prominent green and red luminescence peaks centered at 521 and 655 nm are of variable intensity, while the weak peak of blue emission at 488 nm almost diminishes in the powders with a multiphase composition. Owing to this, the green to red integrated emission ratio inclines as follows: 0.76(S120) → 0.92(S60) → 0.93(S30) → 1.14(S90), while the chromaticity coordinates change in the yellowish green part of the CIE (The Commission International de I'Eclairage) chart in accordance with the drawn line in Fig. 8c. The observed trend suggests that sonofragmentation, reflected by the amorphous phase appearance in the XRPD patterns of S60 and S90, tunes the color saturation (the distance of illuminant white center of the chart), while the re-crystallization of the β phase in S120 shifts back color components toward solid line curve. According to the energy level diagrams presented in Figure 8b, the emission peaks from the visible part of the spectra correspond to the following f–f electronic transitions of the Er^{3+} ion: $^2H_{11/2}$,$^4S_{3/2} \rightarrow {}^4I_{15/2}$(green), $^4F_{9/2} \rightarrow {}^4I_{15/2}$ (red) and $^4F_{7/2} \rightarrow {}^4I_{15/2}$ (blue). Additionally, a weak NIR emission is ascribed to the $^4S_{3/2} \rightarrow {}^4I_{13/2}$ transition. Following the 980 nm excitation, Yb^{3+} absorbs energy and promotes $^2F_{7/2} \rightarrow {}^2F_{5/2}$ transitions. Afterward, it transfers the energy resonantly to the $^4I_{11/2}$ state of the Er^{3+} ion. The supplemental population of this level through direct excitation of Er^{3+} from its ground $^4I_{15/2}$ state enables further energy transfers and the subsequent population of the higher $^4F_{7/2}$ and $^4F_{9/2}$ levels. Electrons excited to the $^4F_{7/2}$ level generate radiative decay to ground $^4I_{15/2}$ or relax non-radiative decay to the $^2H_{11/2}$ and $^4S_{3/2}$ levels, causing further emission of green light through the decay of both levels to the ground $^4I_{15/2}$. In the same time, the intensity of the $^4S_{3/2} \rightarrow {}^4I_{15/2}$ emission is affected by the NIR emission promoted by $^4S_{3/2} \rightarrow {}^4I_{13/2}$ de-excitation. Meanwhile, red emission appears due to $^4F_{9/2} \rightarrow {}^4I_{15/2}$ decay, and is dependent on the non-radiative $^4F_{7/2} \rightarrow {}^4F_{9/2}$ relaxation, as well as $^4I_{13/2} \rightarrow {}^4F_{9/2}$ population. In order to analyze the energy transfer processes in S120, the UC intensity dependence on the pumping power is measured and presented in a log-log diagram,

Fig.8d. The logarithm of the UC emission intensity is linearly proportional to the logarithm of the pumping power with the constant – n, which corresponds to the number of the excitation photons absorbed per emitted photon. Slope values of 1.25 ($^4S_{3/2}\rightarrow{}^4I_{15/2}$) and 1.32 ($^4F_{9/2}\rightarrow{}^4I_{15/2}$) obtained by fitting the data points presented in Fig.9d, confirm that both, green and red emissions are two-photon processes. The superior emission of S120 in comparison to multiphase samples obtained using shorter sonication could be potentially ascribed to the inherit merit of the β phase as well as to the mesocrystal formation through oriented attachment growth during the re-crystallization process. The rational growth of such complex structures through a mild sonochemical process may have a significant impact on their wide potential applications in up/down-conversion science and technology.

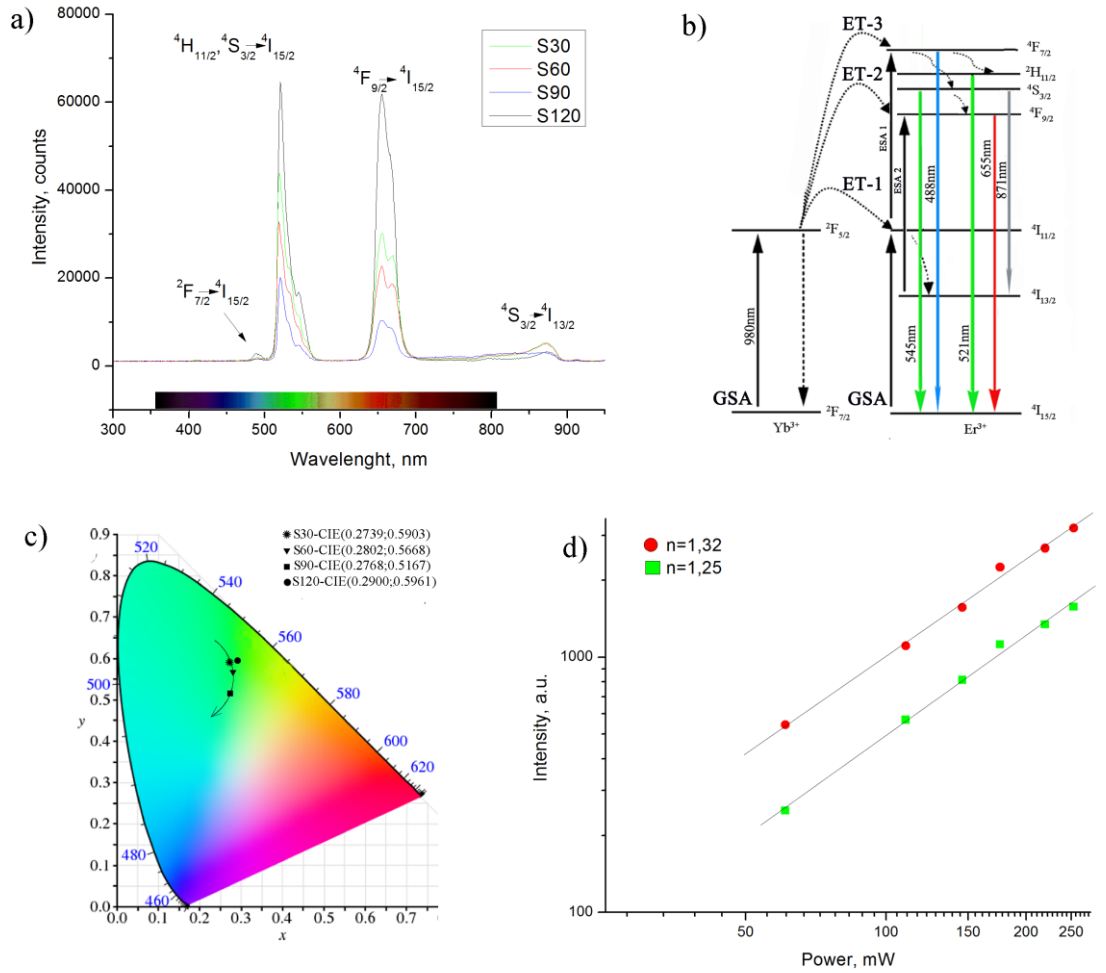

Figure 8. UC emission upon excitation at 980 nm (a); energy level diagram of theYb^{3+}/Er^{3+} couple (b); CIE diagram (c); pump-power dependence of the green and red emission in S120 (d)

Conclusion

In this paper, we demonstrate a facile and mild sonochemical route for the synthesis of pure β $NaYF_4$:Yb,Er phase with a complex structure and a mesocrystal nature. The evolution of Yb,Er doped YF_3 and α $NaYF_4$ phases crystallizing for shorter sonication times was investigated in detail. Based on the analyses, it is concluded that formation of β $NaYF_4$ mesocrystals occurs as a result of the dissolution-recrystallization process and oriented attachment growth. Besides the well-known growth along the [001] plane, a new preferential growth direction perpendicular to (1-12) plane has been detected for β $NaYF_4$:Yb,Er mesocrystals.

Acknowledgements

This work was financially supported by the Ministry of Education, Science and Technological Development of Republic of Serbia, through agreements related to the realization and financing of scientific research work at the Institute of Technical Sciences of SASA and Innovative Centre Faculty of Chemistry Belgrade in 2021, Contract numbers: 451-03-9/2021-14/200175 and 451-03-9/2021-14/200288, respectively. We acknowledge the Multiuser Microscopy Nucleus of COPPE at UFRJ (Brazil) for their support related to the use of electron microscopes. Paula Jardim would also like to acknowledge the National Council for Technological and Scientific Development (CNPq) and Coordenaçao de Aperfeiçoamento de Pessoal de Nível Superior, Brasil (CAPES) for financial support.

References

[1] M. Lin, Y. Zhao, M. Liu, M. S. Qiu, Y. Q. Dong, Z. F. Duan, Y. H. Li, B. Pingguan-Murphy, T. J. Lu, F. Xu, Synthesis of upconversion $NaYF_4:Yb^{3+},Er^{3+}$ particles with enhanced luminescent intensity through control of morphology and phase, J. Mater. Chem. C. 2 (2014) 3671-3676.

[2] H. X. Mai, Y.-W. Zhang, R. Si, Z.-G. Yan, L. D. Sun, L. P. You, C. H. Yan, High-quality sodium rare-earth fluoride nanocrystals: controlled synthesis and optical properties, J. Am. Chem. Soc. 128 (2000) 6426-6436.

[3] M. Jafari, A. Rezvanpour, Upconversion nano-particles from synthesis to cancer treatment: A review, Adv. Powder Technol. 30 (2019) 1731-1753.

[4] I. Dinic, L. Mancic, M. Rabanal, K. Yamamoto, S. Ohara, S. Tamura, K. Tomita; A. M. L. M.Costa, B. Marinkovic, O. Milosevic, Compositional and structural dependence of up-converting rare earth fluorides obtained through EDTA assisted hydro/solvothermal synthesis, Adv. Powder Technol. 28 (2017) 73-82.

[5] M. Vukovic, I. Dinic, M. Nikolic, B. Marinkovic, A. M. L. M. Costa, K. Radulovic, O. Milosevic, L. Mancic, The effects of different polymers and solvents on crystallization of $NaYF_4$:Yb/Er phase, B. Mater. Sci. 43 (2020) 2

[6] R. Qin, H. Song, G. Pan, L. Hu, H. Yu, S. Li, X. Bai, L. Fan, Q. Dai, X. Ren, H. Zhao, T. Wang, Polyol-mediated syntheses and characterizations of $NaYF_4$, $NH_4Y_3F_{10}$ and YF_3 nanocrystals/sub-microcrystals, Mater. Res. Bull. 43 (2008) 2130-2136.

[7] F. Auzel, Upconversion and anti-stokes processes with f and d ions in solids, Chem. Rev. 104 (2004) 139-173.

[8] S. Yang, H. Xia, Y. Jiang, J. Zhang, Y. Shi, X. Gu, J. Zhang, Y. Zhang, H. Jiang, B. Chen, Tm^{3+} doped α-$NaYF_4$ single crystal for 2 μm laser application, J. Alloy. Compd. 643 (2015) 1-6.

[9] H. Suo, X. Zhao, Z. Zhang, T. Li, E. M. Goldys, C. Guo, Constructing multiform morphologies of YF: Er^{3+}/Yb^{3+} up-conversion nano/micro-crystals towards sub-tissue thermometry, Chem. Eng. J. 313 (2017) 65-73.

[10] L. Mancic, A. Djukic-Vukovic, I. Dinic, M. G. Nikolic, M. D. Rabasovic, A. J. Krmpot, A. M.L.M. Costa, B.A. Marinkovic, Lj. Mojovic, O. Milosevic, One-step synthesis of amino-functionalized up-converting $NaYF_4$:Yb,Er nanoparticles for in vitro cell imaging, RSC Adv. 8 (2018) 27429-27437.

[11] P. Zhao, Y. Zhu, X. Yang, X. Jiang, J. Shen, C. Li, Plasmon-enhanced efficient dye-sensitized solar cells using core–shell-structured β-$NaYF_4$:Yb,Er@SiO_2@Au nanocomposites, J. Mater. Chem. 2 (2014) 16523-16530.

[12] H. Xu, B. W. Zeiger, K. S. Suslick, Sonochemical synthesis of nanomaterials, Chem. Soc. Rev. 42 (2013) 2555-2567.

[13] H. M. Xiong, D. G. Shchukin, H. Mohwald, Y. Xu, Y. Y. Xia, Sonochemical synthesis of highly luminescent zinc oxide nanoparticles doped with magnesium(II), Angew. Chem. Int. Edit. 48 (2009) 2727-2731.

[14] Y. Ni, G. Li, J. Hong, Ultrasonic assisted synthesis, characterization and influence factors on monodispersed dumbbell-like YF_3 nanostructures, Ultrason. Sonochem. 17 (2010) 509-514.

[15] J. Lellouche, A. Friedman, A. Gedanken, E. Banin, Antibacterial and antibiofilm properties of yttrium fluoride nanoparticles, Internat. J. Nanomed. 7 (2012) 5611-5624.

[16] D. P. Dutta, S. Warrier, R. Ghildayal, G. Sharma, G. Grover, A. K. Tyagi, Sonochemical synthesis of lanthanide ions doped CeF_3 nanoparticles: potential materials for solid state lighting devices, J. Nanosci. Nanotechno. 9 (2009) 4715-4720.

[17] L. Zhang, W. Li, X. Hu, Y. Peng, J. Hu, X. Kuang, L. Song, Z. Chen, Facile one-pot sonochemical synthesis of hydrophilic ultrasmall LaF_3:Ce,Tb nanoparticles with green luminescence, Prog. Nat.Sci. 22 (2012) 488-492.

[18] C. Yıldırım, Ö. Birer, Ultraviolet upconversion spectra of sonochemically synthesized doped $NaYF_4$ crystals, Chem. Phys. 445 (2014) 46-52.

[19] TOPAS, General Profile and Structure Analysis Sofware for Powder Diffraction Data, V4.2, Bruker AXS GmbH, Karlsruhe, Germany

[20] Y. Feng, B. Shao, Y. Song, S. Zhao, J. Huo, W. Lüa, H. You, Fast synthesis of β-$NaYF_4$:Ln^{3+} (Ln = Yb/Er, Yb/Tm) upconversion nanocrystals via a topotactic transformation route, CrystEngComm. 18 (2016) 7601-7606.

[21] S. Suslick, N. C. Eddingsaas, D. J. Flannigan, S. D. Hopkins, H. Xu, Extreme conditions during multibubble cavitation: Sonoluminescence as a spectroscopic probe, Ultrason. Sonochem. 18 (2011) 842-846.

[22] S. V. Levy, C. R. R. Low, Ultrasound in Synthesis, Springer-Verlag, London UK, 1989.

[23] L. Zhu, C. Fan, W. Fan, J. Yang, W. Huang, J. Zeng, Y. Zhang, X. Cao, X. Cao, Controllable salt-assisted sonochemical synthesis of $Na_xLn_yF_{x+3y}$ (Ln=Sm, Eu) nanostructures, Ceram. Int. 41 (2015) 5032-5040.

[24] M. Ding, D. Chen, S. Yin, Z. Ji, J. Zhong, Y. Ni,C. Lu, Z. Xu, Simultaneous morphology manipulation and upconversion luminescence enhancement of β-$NaYF_4$:Yb^{3+}/Er^{3+} microcrystals by simply tuning the KF dosage, Sci.Rep. 5 (2015) 12745.

[25] M. Ding, C. Lu, L. Cao, Y. Ni, Z. Xu, Controllable synthesis, formation mechanism and upconversion luminescence of β-$NaYF_4$: $Yb^{3+/}Er^{3+}$ microcrystals by hydrothermal process, CrystEngComm, 15 (2013) 8366-8373.

[26] A. B. Bard, X. Zhou, X. Xia, G. Zhu, M. B. Lim, S. M. Kim, M. C. Johnson, J. M. Kollman, M. A. Marcus, S. R. Spurgeon, D. E. Perea, A. Devaraj, J. Chun, J. J. De Yoreo, P. J. Pauzauskie,

A Mechanistic Understanding of Nonclassical Crystal Growth in Hydrothermally Synthesized Sodium Yttrium Fluoride Nanowires, Chem. Mater. 32 (2020) 753-2763.

[27] L. Mino, C. Negri, R. Santalucia, G. Cerrato , G. Spoto, G. Martra, Morphology, Surface Structure and Water Adsorption Properties of TiO2 Nanoparticles: A Comparison of Different Commercial Samples, Molecules 25 (2020) 4605

[28] J. Holsa, T. Laamanen, T. Laihinen, M. Lastusaari, L. Pihlgren, L. C. V. Rodrigues, White up-conversion luminescence of $NaYF_4:Yb^{3+},Pr^{3+},Er^{3+}$, Opt. Mater. 36 (2014) 1627-1630.

[29] T. Laihinen, M. Lastusaarii, L. Pihlgren, L. C. V. Rodrigues, J. Hölsä, Thermal behaviour of the $NaYF_4:Yb^{3+},R^{3+}$ materials, J. Therm. Anal. Calorim. 121 (2015) 37-43.

[30] R. E. Thoma, G. M. Hebert, H. Insley, C. F. Weaver, Phase Equilibria in the System Sodium Fluoride-Yttrium Fluoride, Inorg. Chem. 2 (1963) 1005-1012.

[31] P. P. Fedorova, A. A. Alexandrov, Synthesis of inorganic fluorides in molten salt fluxes and ionic liquid mediums, J. Fluorine Chem. 227 (2019) 109374

[32] A. Kavand, C. Serra, C. Blanck, M. Lenertz, N. Anton, T. Vandamme, Y. Mely, F. Przybilla, D. Chan-Seng , Controlled synthesis of $NaYF_4$:Yb,Er upconversion nanocrystals as potential probe for bioimaging: A focus on heat treatment, ACS Applied Nano Materials, 4, 5 (2021) 5319-5329.

[33] L. Pihlgren, NIR-VIS Up-conversion luminescence in the Yb^{3+} ,Er^{3+} doped Y_2O_2S, ZrO_2 and $NaYF_4$ nanomaterials, PhD thesis, University of Turku, Finland, 2014.